The Astrophysical Journal, 593:1217–1225, 2003 August 20

HELICITY EVOLUTION IN EMERGING ACTIVE REGIONS

Alexei A. Pevtsov
National Solar Observatory,[1] Sacramento Peak, Sunspot, NM 88349; apevtsov@nso.edu

Vasily M. Maleev[2]
Saint Petersburg State University, Petrodvorets, Saint Petersburg, Russia; vasya@astro.spbu.ru

and

Dana W. Longcope
Department of Physics, Montana State University, Bozeman, MT 59717-3840; dana@physics.montana.edu
Received 2003 March 4; accepted 2003 May 7

ABSTRACT

We study the evolution of twist and magnetic helicity in the coronal fields of active regions as they emerge. We use multiday sequences of *Solar and Heliospheric Observatory* Michelson Doppler Interferometer magnetograms to characterize the region's emergence. We quantify the overall twist in the coronal field, α, by matching a linear force-free field to bright coronal structures in EUV images. At the beginning of emergence, all regions studied have $\alpha \simeq 0$. As the active region grows, α increases and reaches a plateau within approximately 1 day of emergence. The inferred helicity transport rate is larger than differential rotation could produce. Following the 2000 work of Longcope & Welsch, we develop a model for the injection of helicity into the corona by the emergence of a twisted flux tube. This model predicts a ramp-up period of approximately 1 day. The observed time history $\alpha(t)$ is fitted by this model assuming reasonable values for the subphotospheric Alfvén speed. The implication is that helicity is carried by twisted flux tubes rising from the convection zone and transported across the photosphere by spinning of the poles driven by magnetic torque.

Subject headings: Sun: corona — Sun: magnetic fields — sunspots

1. INTRODUCTION

It is widely accepted now that the magnetic field of active regions is generated by the dynamo operating at the bottom of the convection zone. The dynamo flows transfer their kinetic helicity [$H_k = \int (\nabla \times \boldsymbol{v}) \cdot \boldsymbol{v}\, dD$] into magnetic field helicity (magnetic, $H_m = \int (\nabla \times \boldsymbol{A}) \cdot \boldsymbol{B}\, dD$, or current, $H_c = \int (\nabla \times \boldsymbol{B}) \cdot \boldsymbol{B}\, dD$, where $\boldsymbol{A}$, $\boldsymbol{B}$, and $\boldsymbol{v}$ are the magnetic vector potential, magnetic induction, and velocity, accordingly). Once the magnetic field crosses the photosphere, helicity manifests itself via a nonzero twist or electric currents. Indeed, most, if not all, active regions exhibit some degree of twist in their photospheric magnetic fields (e.g., Pevtsov, Canfield, & Metcalf 1995; Bao & Zhang 1998). Some of these electric currents should propagate up into the corona, since the observations show a good correlation between the photospheric and coronal force-free field α-coefficient (Pevtsov, Canfield, & McClymont 1997; Burnette, Canfield, & Pevtsov 2003). The twist observed in the photosphere may be of subphotospheric origin (e.g., Longcope et al. 1999) or due to (near) surface motions (e.g., differential rotation/shear motions; DeVore 2000; Chae 2001). Numerical simulations have established that a small amount of twist is necessary for a flux tube rising through the convection zone to survive as an entity (Emonet & Moreno-Insertis 1998; Fan, Zweibel, & Lantz 1998). Observations also indicate that the magnetic field emerges carrying a nonzero twist (Leka et al. 1996; Portier-Fozzani et al. 2001; Grigoryev & Ermakova 2002), which implies that at least some fraction of the photospheric helicity may be generated below the photosphere.

Berger & Field (1984) showed that the magnetic helicity flux into the solar atmosphere can be separated into two components, one due to vertical advection of the twisted magnetic field through the photosphere and one due to "braiding" of fields by differential rotation or other large-scale horizontal motions. The contribution of differential rotation to the helicity budget was quantified for active regions (DeVore 2000) and for the large-scale solar magnetic field (Berger & Ruzmaikin 2000). The braiding contribution was observationally measured (Chae 2001; Moon et al. 2002) and found to greatly exceed the contribution that might have been provided by differential rotation alone. This higher level of helicity transport is also required to account for the helicity loss by coronal mass ejections, which has been found to greatly exceed the production possible by differential rotation (Démoulin et al. 2002; Green et al. 2002).

Helicity flux studies therefore imply that magnetic helicity transport into active region magnetic fields results, at least in part, from local photospheric flow fields. Since the active region magnetic helicity exhibits a correlation with latitude (Pevtsov et al. 1995), these local flows must be arranged to inject (preferentially) negative helicity into northern regions and positive helicity into southern fields. It is common to assume that photospheric flows will be affected very little by the magnetic field itself, since the *average* plasma β is small. This means that local photospheric flows of nonmagnetic origin are responsible for injecting helicity into the active region corona.

Longcope & Welsch (2000) reasoned, however, that vortical motions responsible for helicity injection cannot be driven by pressure gradients and cannot easily be produced

[1] The NSO is operated by the Association of Universities for Research in Astronomy, Inc., under cooperative agreement with the National Science Foundation.

[2] NSO 2002 Summer Research Assistant.

by coupling motions of nonmagnetic plasma to the active region itself. Moreover, any magnetic torques arising from the active region's subphotospheric field cannot be countered by pressure gradients. They demonstrated this in a model wherein a twisted subphotospheric flux tube drove photospheric flows to transport helicity into the active region above it. These flows were components of a torsional Alfvén wave that transported helicity along the length of the flux tube. The model made the further prediction that an emerging active region would develop twist on a timescale of roughly 1 day: the Alfvén travel time over the subphotospheric axis containing the helicity required by the coronal field.

The time evolution of the coronal twist during the emergence of an active region can be used to infer the mechanism driving the photospheric flows that transport magnetic helicity. Flows of nonmagnetic origin would drive passive magnetic fields, injecting helicity at a rate unrelated to the active region's emergence. There is no reason to expect these flows to be coordinated with emergence, so almost any time history would be possible. On the other hand, if the flows were driven by magnetic torques, the coronal twist would evolve similarly in every emerging region: beginning small or zero initially and ramping up to a final value. The timescale of the ramp-up would be the longer of the subphotospheric Alfvén time and the polarity separation time (Longcope & Welsch 2000).

Based on observations of the coronal twist evolution during the emergence of six different active regions, we conclude that helicity is injected by magnetically driven flows. We find that each active region's twist exhibits the characteristic evolution described above and can even be fitted to a quantitative model of twist evolution. In § 2 we describe our data and how it is used to measure coronal twist and other aspects of flux tube emergence. Section 3 presents the results of these observations and describes the generic active region development and coronal twist evolution. Section 4 presents a model for the coupling of helicity from a twisted flux tube to an emerging active region. This model is then fitted numerically to the observed twist evolutions. This fitting yields an estimate of the subphotospheric flux tube's Alfvén velocity at a depth of 5–10 Mm. Section 5 examines the implications of these results on theories of the generation and transport of magnetic helicity.

2. DATA

Our ultimate objective is to quantify the magnetic helicity in the coronal fields of active regions as they emerge. To actually calculate the (relative) helicity would require a three-dimensional grid of vector field measurements throughout the corona; a measurement of this kind has never been made. The alternative is either to calculate the helicity of a model coronal field (Démoulin et al. 2002) or to integrate the photospheric helicity flux, which is found from surface maps of all three components of the magnetic field and the plasma velocity (Kusano et al. 2002). High time cadence vector magnetic field measurements of emerging active regions are extremely rare (a point to which we return below), so we are forced to estimate the magnetic helicity from a model magnetic field constructed using only line-of-sight field measurements.

The magnetic field measurements we use for this purpose are full-disk, line-of-sight magnetograms from the Michelson Doppler Imager (MDI; Scherrer et al. 1995) on board the *Solar and Heliospheric Observatory* (*SOHO*; Domingo, Fleck, & Poland 1995). These magnetograms have a spatial resolution of $1\farcs98$ pixel^{-1} and are available at a time cadence of 96 minutes for virtually the entire period since *SOHO* was launched.

The simplest magnetic model that can be constructed from these measurements is a linear force-free field (LFFF) satisfying $\nabla \times \boldsymbol{B} = \alpha \boldsymbol{B}$, where α is the single free parameter of the model. Unfortunately, not even this simple model can be constrained using line-of-sight magnetograms alone, so we must introduce at least one piece of additional data.

We constrain the parameter α by comparing field lines from the model with EUV images of the active region. For this comparison we use 195 Å (Fe XII) full-disk images from the EUV Imaging Telescope (EIT; Delaboudinière et al. 1995) on board *SOHO*, which has a resolution of $2\farcs63$ pixel^{-1}. We require that the MDI and EIT observations be within a few minutes of each other to obviate the need to correct for solar rotation when comparing the two data sets. The LFFF matching the line-of-sight field is found for a specified value of α, and then numerous field lines are plotted over the co-aligned EIT image. This procedure is repeated for a range of α-values, and that value is selected whose model field lines most resemble the bright coronal structures of the EIT image.

This fitting method yields a parameter α that characterizes the twist in the coronal magnetic field of the active region as a whole. The method seems subjective, since an observer must decide when the field lines best fit the bright EUV structures. Furthermore, the method tacitly assumes that the active region field has a single sense of twist and that structures visible in EIT 195 Å images actually follow magnetic field lines. There is evidence, however, in a study by Burnette et al. (2003), that the value of α so found is a good proxy for more accurate measures of the overall magnetic twist. Burnette et al. calculated magnetic twist in two independent ways for each of 34 mature active regions observed with both vector magnetograms and *Yohkoh* soft X-ray images. One measure of twist, which they call α_c and which is identical to our α, was found by fitting a LFFF to the vertical field and adjusting α to best match the bright features in the coronal image. An independent twist parameter was provided by $\alpha_{\rm best}$, which involves all three of the measured photospheric field components. This measure of twist, introduced by Pevtsov et al. (1995), has been used extensively to characterize the twist in active magnetic fields (Pevtsov et al. 1997; Longcope et al. 1999; Longcope & Pevtsov 2003). Burnette et al. (2003) found that the two different measures of average twist were highly correlated (Spearman rank correlation $\rho = 0.71$) and fitted a line $\alpha_c = (0.91 \pm 0.13)\alpha_{\rm best}$. We therefore conclude that α_c can be used as a proxy for $\alpha_{\rm best}$ in those cases in which vector magnetograms are unavailable.

We began by selecting a set of emerging active regions on which to perform our study. Using Solar-Geophysical Data monthly reports, we identified several regions that emerged east of the central meridian. Next, we used MDI and EIT records to select those emerging regions that were well observed by both instruments. Table 1 lists the six active regions satisfying this criterion that we use in our study.

The coronal fitting method was then applied to each pair of MDI/EIT images to yield a value of α at that time. The active region was further characterized by the flux in each

TABLE 1
SELECTED ACTIVE REGIONS

NOAA	Date (Beginning)	Latitude (deg)	CMD_B (deg)	CMD_E (deg)
8582	1999 Jun 10	26.5	−50.6	−5.8
8738	1999 Oct 20	18.7	−39.6	−13.1
8768	1999 Nov 14	16.3	−57.7	−12.8
8817	2000 Jan 3	25.7	−33.3	15.4
9139	2000 Aug 19	9.9	−43.3	−5.4
9193	2000 Oct 11	9.1	−4.7	25.5

polarity and the separation d between poles. On each magnetogram, we visually located points approximating the positions of the negative and positive polarities. The contiguous region above a fixed threshold (50 G) that included the "pole point" was defined as the polarity region. The total flux in this region was the pole's flux, and its center of figure (weighted by the unsigned magnetic flux) was its location. The image coordinates of the polarity centers were converted into heliospheric coordinates, and the separation calculated in heliographic degrees; this distance was then converted to megameters. In all cases the magnetic flux and its area grew steadily as the active region emerged and evolved.

Uncertainties in α were estimated by using the late, stable period (when the coronal images did not change significantly) in each active region's evolution. Assuming the coronal field was in fact static during this period, each measurement of α is an independent measurement of the same quantity, and the standard deviation $\sigma\alpha$ is an estimate of the measurement error. We apply this estimate of uncertainties to α throughout the emergence of that particular active region. Uncertainties in total flux and footpoint separation are extremely small, since each value arises from the sum of 100 or more pixels.

3. EVOLUTION OF ACTIVE REGIONS AND THEIR TWIST

Figure 1 shows the early evolution of emerging NOAA active region 9139. The magnetic field associated with the region can first be identified around August 19, 12:47 UT (Fig. 1*a*), and within a day it develops into a distinct bipolar region. Figure 2 shows the evolution of the magnetic parameters of this region, i.e., twist α, polarity separation d, magnetic flux, and total area. Polarity separation and magnetic flux are corrected for projection. As the active region develops, both its total area and magnetic flux grow. The polarity separation increases and reaches a plateau $\approx$1.5 days after the beginning of emergence. On the other hand, the α-coefficient increases much faster, and it reaches the plateau in less than a day. This behavior is reminiscent of the "slow emergence" scenario in Longcope & Welsch (2000). Figure 3 gives an example of another emerging region, NOAA AR 8817. As with NOAA AR 9139, the evolution of this region corresponds to the "slow emergence" scenario, although the evolution of α is much noisier as compared to Figure 2.

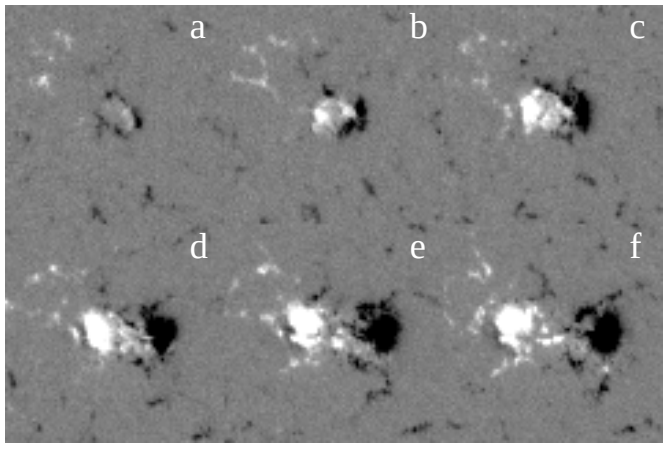

FIG. 1.—Emergence of active region NOAA AR 9139 on (*a*) 2000 August 19, 1247 UT, (*b*) 2000 August 19, 2047 UT, (*c*) 2000 August 20, 0447 UT, (*d*) 2000 August 20, 1247 UT, (*e*) 2000 August 20, 2047 UT, and (*f*) 2000 August 21, 0447 UT. White indicates positive polarity, while black indicates negative.

Not all active regions exhibit a monotonic increase in α and polarity separation as in Figure 2, e.g., in the case of NOAA AR 8768 (Fig. 4), both the polarity separation and α decreased after an initial period of growth. However, on close examination of magnetograms of this region, we found that another region was emerging in close proximity. Thus, we believe that our method of fitting overall coronal structure to a photospheric magnetogram may have been affected by this new flux emergence.

4. A MODEL OF EMERGENCE

A model of an emerging twisted flux tube was developed by Longcope & Welsch (2000). They began by assuming the evolution to be slow enough that the coronal field remains in force-free equilibrium characterized by its total relative helicity H_R. For a constant-α field with footpoint separation d, the relative helicity within the active region is approximately

$$H_R \simeq \frac{\Phi^2}{2\pi}\alpha d \,, \tag{1}$$

where Φ is the net magnetic flux in either pole. If no helicity were added, then the magnitude of α would decrease as d increased; in fact, α is observed to increase along with d.

Relative helicity is added to or removed from the corona by motion of the photospheric polarities. Approximating the polarities as small, unipolar patches, the change in relative helicity is (Berger & Field 1984; Longcope & Pevtsov 2003)

$$\frac{dH_R}{dt} = -\frac{\Phi^2}{2\pi}(\omega_+ + \omega_-) \,, \tag{2}$$

where ω_+ and ω_- are the angular velocities with which the positive and negative polarities spin about the vertical.

Each photospheric polarity is the terminus of a flux tube extending into the convection zone. A spinning motion of this terminus must arise from a torque exerted either by the flux tube beneath or by the photospheric plasma surrounding it. We neglect the latter possibility because of numerous uncertainties in the process of coupling the magnetic and nonmagnetic components at high Reynolds number (Longcope & Pevtsov 2003). We therefore consider only effects internal to the flux tube. The dynamics of a twisted flux tube have been modeled under the approximation that

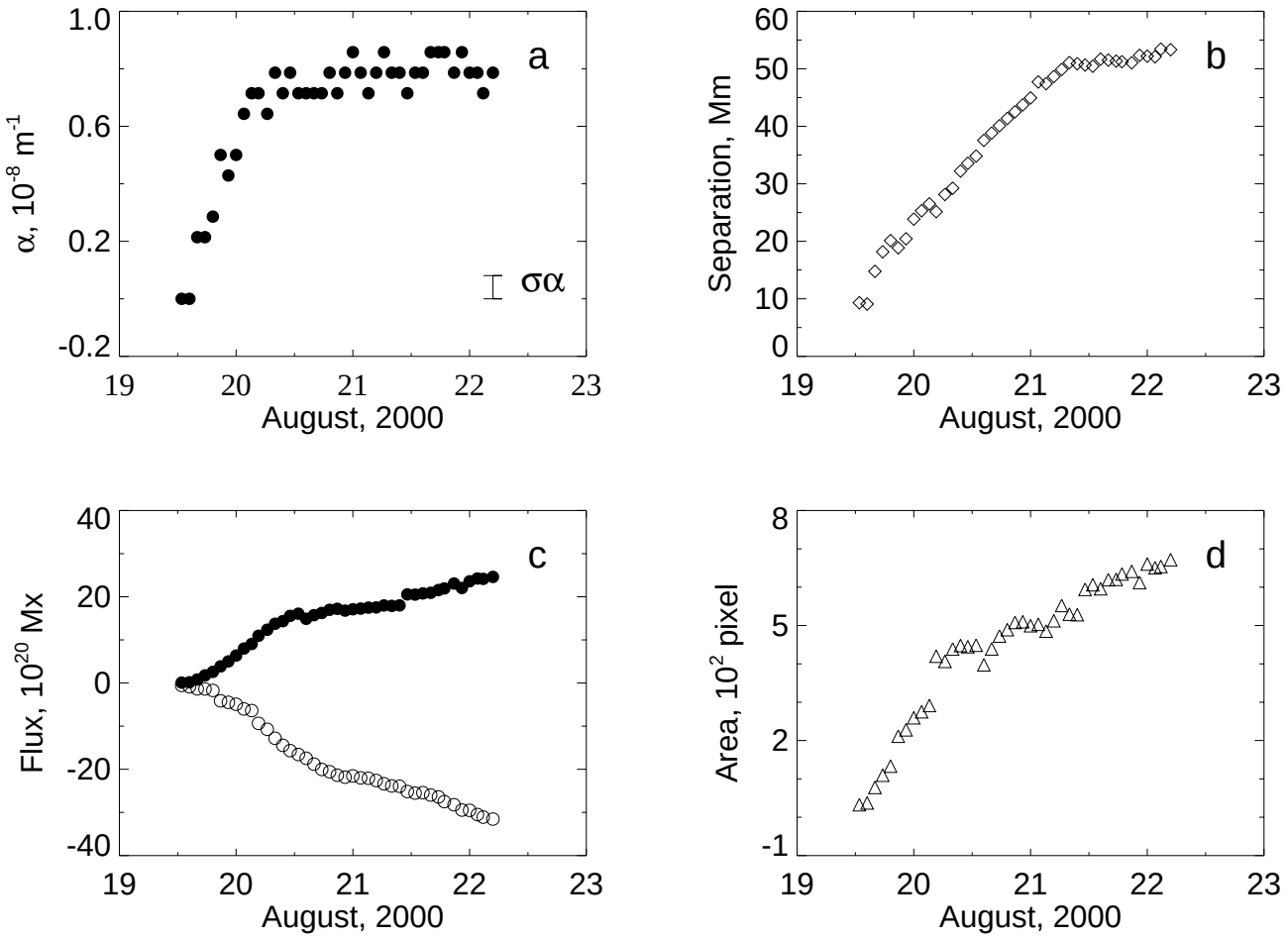

FIG. 2.—Evolution of magnetic parameters of NOAA AR 9139: (*a*) α, (*b*) polarity separation, (*c*) magnetic flux, and (*d*) total area

its cross section is sufficiently thin (Longcope & Klapper 1997).

We henceforth adopt this thin flux tube approximation and parameterize each axis by a length coordinate s increasing toward the photosphere at $s = 0$. The field lines twist about the axis at a local pitch $q(s)$, such that a given field line will wrap once over a length $\Delta s = 2\pi/|q|$ in a right-handed helix for $q > 0$ and a left-handed helix for $q < 0$. The material in the tube spins about the axis at angular velocity $\omega\hat{\boldsymbol{s}}$, where $\hat{\boldsymbol{s}}$ is the axial tangent vector. Neglecting the motion of

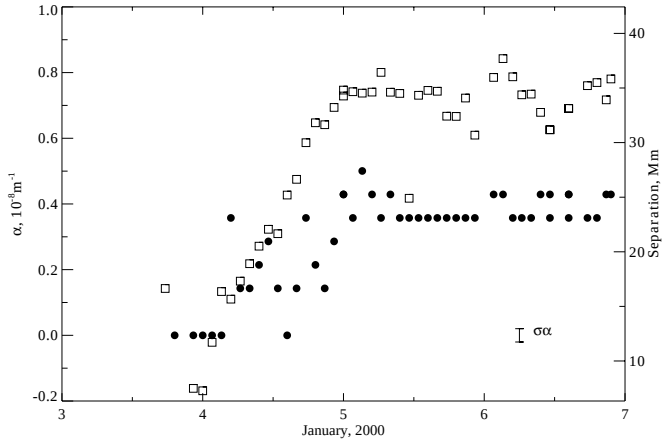

FIG. 3.—NOAA AR 8817. Filled circles show α, and squares show polarity separation.

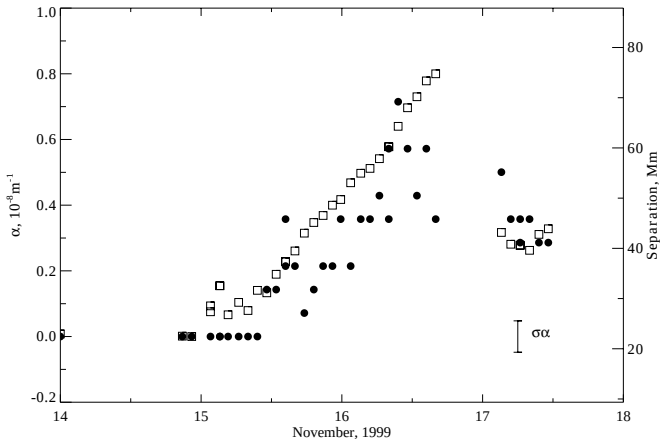

FIG. 4.—NOAA AR 8768. Filled circles show α, and squares show polarity separation.

the axis itself, the twist and spin satisfy the telegrapher's equations (Longcope & Klapper 1997; Longcope & Pevtsov 2003),

$$\frac{\partial q}{\partial t} = \frac{\partial \omega}{\partial s} , \tag{3}$$

$$\frac{\partial \omega}{\partial t} = v_{\rm A}^2 \frac{\partial q}{\partial s} , \tag{4}$$

where $v_{\rm A}$ is the Alfvén speed along the tube's axis.

Under the further assumption of uniform Alfvén speed, equations (3) and (4) admit solutions in the form of arbitrary incident and reflected waveforms $w_i(t)$ and $w_r(t)$:

$$q(s,\ t) = w_r\left(t + \frac{s}{v_{\rm A}}\right) + w_i\left(t - \frac{s}{v_{\rm A}}\right) , \tag{5}$$

$$\omega(s,\ t) = v_{\rm A}\left[w_r\left(t + \frac{s}{v_{\rm A}}\right) - w_i\left(t - \frac{s}{v_{\rm A}}\right)\right] . \tag{6}$$

A flux tube in uniformly twisted equilibrium requires a continual reflection of the photospheric boundary so that $w_r = w_i = q/2$.

The twisted flux tube carries an internal, axial current $I = 2q\Phi$ along its field lines and an opposing return current at its surface. To maintain force balance across the photosphere, the interior current must pass into the corona so that $\alpha = 2q$ (Longcope & Welsch 2000). This condition at $s = 0$ is what determines the reflection of torsional waves off the photospheric surface: $w_r(t) = \alpha(t)/2 - w_i(t)$. According to equation (6), the observed photospheric motion is a combination of the incident and reflected waves. Using the expression for the reflection yields the photospheric angular velocities

$$\omega_{\pm} = \tfrac{1}{2} v_{\rm A} \alpha - 2 v_{\rm A} w_{i,\pm} , \tag{7}$$

where $w_{i,+}$ and $w_{i,-}$ are the waveforms incident on the positive and negative poles, respectively. Thus, the photospheric sources will spin if the twist incident from below is not properly matched to the coronal twist α.

Using the boundary condition in equation (7) in the helicity evolution, equation (2) yields an expression for the evolution of α:

$$2\pi\Phi^{-2}\frac{dH_R}{dt} = d\dot{\alpha} + \alpha\dot{d} = -v_{\rm A}\left(\alpha - 2w_{i,+} - 2w_{i,-}\right) . \tag{8}$$

If both polarities are anchored to flux tubes that were initially uniformly twisted with $q = \bar{q}$, then the incident waves from each side will be $w_{i,\pm} = \bar{q}/2$. Under this assumption the coronal twist will evolve according to

$$\frac{d\alpha}{dt} + \frac{\dot{d}}{d}\alpha = -\frac{v_{\rm A}}{d}(\alpha - \bar{\alpha}) , \tag{9}$$

where $\bar{\alpha} \equiv 2\bar{q}$ is the asymptotic value for the coronal twist α.

4.1. *Fitting the Data*

In general, the observed active regions begin with no measurable twist at the instant of emergence t_0, so we take $\alpha(t_0) = 0$. Observations strongly suggest that the emergence process can be modeled as a linear increase in separation beginning with $d(t_0) = d_0$. The separation increases at constant rate $\dot{d}$ until a time t_1, after which d remains constant:

$$d(t) = \begin{cases} d_0 + \dot{d}(t - t_0), & t_0 \le t \le t_1 , \\ d_0 + \dot{d}(t_1 - t_0) \equiv d_1, & t_1 < t . \end{cases} \tag{10}$$

The solution to equation (9) for the emergence period, $t_0 \le t \le t_1$, is

$$\alpha = \bar{\alpha}\frac{\nu}{\nu + 1}\left[1 - \left(\frac{d}{d_0}\right)^{-(\nu+1)}\right] , \tag{11}$$

where $\nu \equiv v_{\rm A}/\dot{d}$. This form for $\alpha(t)$ differs from that derived by Longcope & Welsch (2000), who assumed a different form for $d(t)$.

During the postemergence period, where $\dot{d} = 0$ and $d = d_1$, α approaches $\bar{\alpha}$ exponentially with time constant $d_1/v_{\rm A}$. The explicit form of the observed coronal twist for both periods is

$$\alpha(t) = \begin{cases} \bar{\alpha}\dfrac{\nu}{\nu + 1}\left\{1 - \left[1 + \dfrac{\dot{d}}{d_0}(t - t_0)\right]^{-(\nu+1)}\right\}, & t_0 \le t \le t_1 , \\ \bar{\alpha} + (\alpha_1 - \bar{\alpha})\exp\left[\dfrac{-v_{\rm A}(t - t_1)}{d_1}\right], & t_1 < t , \end{cases} \tag{12}$$

where $\alpha_1 = \alpha(t_1)$.

The data described in § 3 (except for AR 8738, for which $\alpha \simeq 0$) are fitted to the above model in a two-step procedure. First, the separation curve is fitted to the model in equation (10). The beginning and ending times for emergence, t_0 and t_1, are identified by inspection. Then, d_0 and $\dot{d}$ are determined by fitting the measured values of d to a linear function of t (over the interval $t_0 \le t \le t_1$) using linear least-squares. With these values fixed, ν and $\bar{\alpha}$ are the only free parameters remaining in expression (12). Measured values of α from times $t < t_1$ are fitted to that functional form using nonlinear least-squares. Figure 5 shows typical fits, AR 9139 and AR 8587, along with the somewhat problematic case of AR 9193. The parameters found from fitting all data sets are listed in Table 2.

The instrumental uncertainties in the separation d are expected to be extremely small, as discussed in § 2. We therefore use the linear fit itself to estimate the uncertainties in the parameter $\dot{d}$ (Bevington & Robinson 1992). These turn out to be extremely small, owing to the remarkably linear behavior in $d(t)$. As described in § 2, uncertainties in the twist parameter α are estimated by assuming the final phase in its time evolution is a constant value plus measurement errors. These uncertainties are used to estimate uncertainties in the fitting parameters, ν and $\bar{\alpha}$, by the Monte Carlo technique: 1000 synthetic data sets, measurements plus additional random noise, are constructed and then fitted (Press et al. 1986). These uncertainty estimates are larger and more realistic than the classical estimates defined by $\Delta\chi^2 \le 1$. The uncertainty in $v_{\rm A}$ is found by adding in quadrature the relative errors in $\dot{d}$ and ν.

The model fits all of the data sets well, as typified by Figure 5. Values of χ_ν^2 are all above unity, as expected for an imperfect model of reality. It might also be the case that our estimates of $\sigma\alpha$ are systematically small, since they are made during the late quiescent phase of evolution. For example, Figure 3 shows much more point-to-point scatter in the

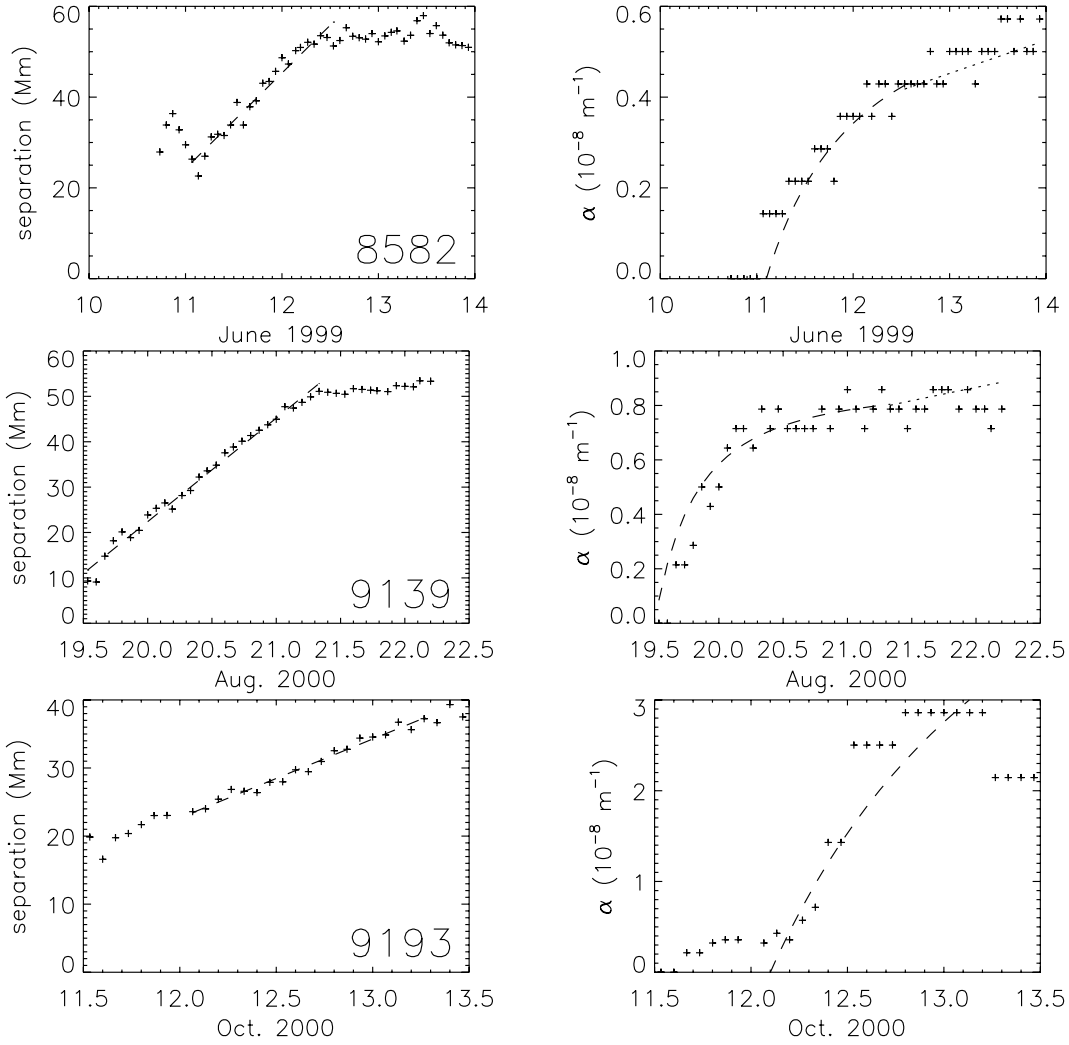

FIG. 5.—NOAA AR 8582 (*top*), NOAA AR 9139 (*middle*), and NOAA AR 9193 (*bottom*) fitted to the emergence model. The left panels show measured separation d (*plus signs*) and the fit (*dashed line*) out to t_1. The right panels show the measured twist α (*plus signs*) and the fit (*dashed line*) done for $t_0 \le t \le t_1$. The dotted line shows the model for evolution after t_1, for which there are no remaining free parameters.

early phase than the later phase from which $\sigma\alpha$ was found. This may be an important factor in the large value of χ^2_ν for NOAA AR 8817.

From expression (11) it can be seen that α_1 is smaller than $\bar{\alpha}$ at least by a factor $\nu/(\nu+1)$. It is therefore not surprising that the parameter $\bar{\alpha}$ found from each fit exceeds, by at least a factor of 2, the largest measured values of α. According to the postemergence curve, $\alpha(t)$ should approach $\bar{\alpha}$ on a timescale d_1/v_A, typically about 5 days in these cases. Thus, we observe very little change in α over the 1–2 days observed after the active region has completely emerged.

The greatest discrepancy between $\bar{\alpha}$ and α_1, a factor of 8, was found in AR 9193 (bottom of Fig. 5). This active region was notable for its complex twist history, which included a half-day latency following emergence and a decrease while $\dot{d}$

TABLE 2
FITTED MODEL PARAMETERS

NOAA	$t_1 - t_0$ (days)	$\dot{d}$ ($m\,s^{-1}$)	d_0 (Mm)	$\bar{\alpha}$ ($10^{-8}\,m^{-1}$)	ν	v_A ($m\,s^{-1}$)	χ^2_ν
8582	1.3	244 ± 12	25.65	3.34 ± 0.88	0.26 ± 0.07	63 ± 16	3.9
8738	...	...	...	0	...	...	...
8768	1.3	376 ± 8	27.06	1.71 ± 0.76	0.52 ± 0.22	197 ± 83	2.2
8817	1.0	229 ± 9	26.79	2.17 ± 0.27	0.41 ± 0.05	94 ± 11	8.2
9139	1.8	264 ± 6	11.74	2.36 ± 0.17	0.60 ± 0.04	158 ± 11	2.4
9193	1.0[a]	134 ± 5	23.45	22.06 ± 1.45	0.44 ± 0.02	59 ± 4	5.8

[a] Here t_0 and t_1 reflect the phase of increasing α.

was still positive. We consider the implications of this complex evolution in § 5.

The case of AR 8738, $\alpha(t) \simeq 0$, can be fitted trivially by taking $\bar{\alpha} = 0$. This reflects the fact that if an untwisted flux tube emerges, the coronal field will remain potential (current free). This degenerate case provides no information about ν or v_A.

The ratio $\nu = v_A/\dot{d}$ is considered a free parameter in our fitting. This means that we are using coronal observations to "measure" the subphotospheric Alfvén speed. This is a reasonable approach, considering that there are no direct means of observing the magnetic field at depths of 5–10 Mm. Furthermore, our model assumes the subphotospheric Alfvén speed to be constant, for simplicity. The value of v_A found by our fitting should thus be interpreted as an *average* subphotospheric Alfvén speed. It is rather encouraging that all five cases considered yield similar Alfvén speeds, roughly 100 m s^{-1}. We consider below the reasonableness of this value for flux tubes beneath active regions.

5. DISCUSSION

The foregoing analysis quantified the overall twist in the coronal field by extrapolating a LFFF from photospheric magnetograms and adjusting α by comparisons of field lines with coronal images. While a more straightforward and accurate measurement of α is possible using vector magnetograph (VMG) data (Pevtsov et al. 1995), this is not practical for the present study. One difficulty with its application is that all VMGs are currently on ground-based telescopes and therefore cannot provide continuous multiday observations. Another difficulty is that vector magnetograms of the very early stages of emerging active regions are almost nonexistent.

One particular observation does exist with which we might check our findings. Figure 6 shows very rare observations (by the Haleakala Stokes Polarimeter; Mickey 1985) of an emerging region close to a preexisting leading polarity sunspot. We used the vector magnetograms to derive a different measurement of the overall twist, α_{best}, following Pevtsov et al. (1995). Computing it separately for the existing flux (*filled circles*) and emerging fluxes (*open circles*) shows an evolution of α_{best} for the emerging flux (Fig. 6) similar to that exhibited by the coronal-fit α in regions from our study, e.g., Figures 2 and 3. The twist α_{best} in the emerging features (*open circles*) increases in magnitude (it is negative) from August 17 until it peaks on August 19. This coincides with the separation of the polarities (*squares*). Thus, we find that a more accurate estimate of the twist shows the same pattern of evolution as do our coronal-fit measurements. This conforms to the expectation born of the work by Burnette et al. (2003), which established that α could be used as a proxy for α_{best}.

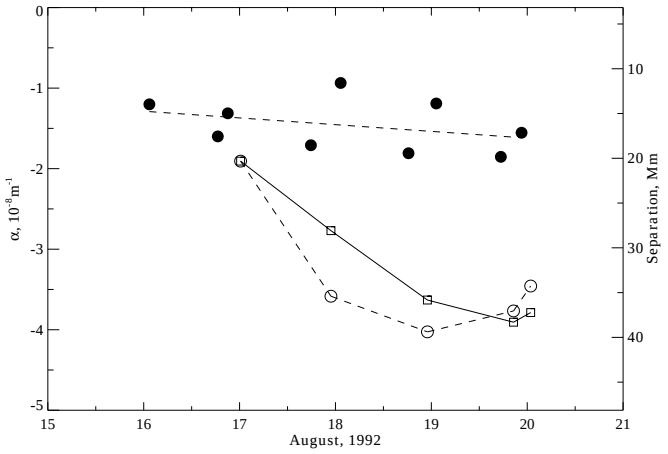

FIG. 6.—Evolution of an emerging region at the trailing portion of NOAA AR 7260. Circles indicate α_{best} measured from vector magnetograms. Filled circles show the existing region (the leading sunspot of NOAA AR 7260), and open circles show the emerging portion. Squares show the polarity separation of the emerging section.

Using the coronal-fitting technique, we compiled data for six different emergences. These showed a general trend for the coronal twist to increase at roughly the same time as the polarities separated. It is notable that the twist can reach a plateau either before or after the separation does. In four cases, α plateaus earlier than the polarity separation, while in one case (NOAA AR 8582), α plateaus later. (In the sixth case, NOAA AR 8738, we find no change in α, even as the active region grows.) This range of behavior is not easily reconciled with simple scenarios of helicity injection but *is* predicted by the twist injection model (Longcope & Welsch 2000).

In all cases studied, the magnetic field appears to be untwisted at the beginning of emergence; in all cases but one (AR 9193), α increases during emergence and reaches a plateau within ~0.8–1.7 days. The active region has therefore gained helicity during the process of emergence. We can estimate the final helicity of each active region from equation (1), using α- and d-values already found and defining Φ as half the unsigned flux of the active region.[3] The resulting helicities, listed in Table 3, are typically 10^{41} Mx^2, comparable to active region helicities found by other means (Green et al. 2002).

The helicity flux through the photospheric surface ($z = 0$) is

$$\frac{dH_R}{dt} = 2\int (\boldsymbol{A}_p \cdot \boldsymbol{B}_\perp) v_z \, dx \, dy - 2\int (\boldsymbol{A}_p \cdot \boldsymbol{v}_\perp) B_z \, dx \, dy \ , \quad (13)$$

where $\boldsymbol{A}_p$ is the vector potential of a potential field matching the vertical photospheric field B_z (Berger & Field 1984). The first and second terms on the right-hand side of this expression are contributions due to vertical motions v_z (emergence) and horizontal motions $\boldsymbol{v}_\perp$ (braiding). Vertical

[3] The magnetic flux was corrected by a factor of 0.64 following Berger & Lites (2003), who showed that the MDI calibration underestimates the true flux densities by a factor of 0.64 (plage) and 0.69 (sunspots).

TABLE 3
CHARACTERISTICS OF ACTIVE REGION EMERGENCE IN OUR SAMPLE

NOAA	Flux (10^{20} Mx)	Helicity (10^{41} Mx^2)	dH_R/dt (10^{41} Mx^2 day^{-1})
8582	30	4.0	2.3
8738	...	...	...
8768	13	1.3	1.4
8817	17	0.9	0.9
9139	44	12.7	1.6
9193	20	10	1.1

motions transport helicity by advecting a twisted field across the photospheric surface. If this mechanism were dominant, we would expect the twist of the coronal field to remain at a constant value, $\alpha \sim \bar{\alpha}$, throughout the emergence process. In this scenario, H_R increases in proportion to Φ^2 as pretwisted flux is moved into the corona. Our data show, to the contrary, that α begins small and increases at the same time Φ is increasing. Thus, we conclude that helicity is transported into the corona primarily by horizontal photospheric motions.

The horizontal photospheric motions responsible for helicity transport can have two basic causes. They may be flows of the unmagnetized plasma that affect an apparently passive magnetic flux, or they may be flows driven by magnetic forces. It is often assumed that magnetic forces will not be effective in the photosphere and convection zone where β is typically large. Therefore, active region fields are often modeled as if their lower boundary were "driven" by prevailing motions such as differential rotation.

DeVore (2000) applied the passive-advection approach to calculate the helicity flux into a bipolar active region whose photospheric footpoints moved according to differential rotation. The resulting helicity flux depended on the latitude, separation, and *tilt angle* of the bipole. If all of these factors were optimally chosen, the helicity flux could be as large as $dH_R/dt \simeq 3 \times 10^{-3}\Phi^2$ day^{-1}. When applied to our sample, this value is smaller, typically by an order of magnitude, than the helicity flux we actually observe. Thus, we can reject differential rotation as a possible source of helicity injection.

The ineffectiveness of differential rotation does not mean that photospheric motions cannot inject significant helicity. Chae (2001) and Nindos & Zhang (2002) both used local correlation tracking techniques to measure horizontal motions and thereby compute helicity fluxes. The helicity injection rates they computed were significantly larger than differential rotation could supply. Indeed, the flow patterns found by the tracking technique are highly localized and appear unrelated to differential rotation. These observations cannot, however, shed light on whether the observed motions are driven by magnetic or nonmagnetic forces.

The clear relationship between $\alpha(t)$ and $d(t)$ observed strongly in all cases suggests that helicity is injected by flows driven by the emergence itself. Had the field instead evolved under the influence of existing local flows, there would be no reason to expect the helicity injection to be related to the emergence, as we observe it to be. Thus, we propose that magnetic forces within the emerging active region drive the flows that transport helicity into the corona.

We propose a model of these magnetically driven flows and find that it fits every one of our observed emergences. In this model the twist from the flux tube propagates as torsional Alfvén waves, ultimately supplying the coronal field with helicity. The natural timescale for this process is governed by the Alfvén speed within the tube and the rate of polarity separation. We fit the observations by tuning the Alfvén speed, as shown in Table 2. Since the ramp-up time for α is typically 1 day, the torsional Alfvén waves will have propagated from that depth. This is a depth of $\sim$8 Mm, using the inferred speed of $v_A \sim 100$ m s^{-1}. At this depth, $\rho \simeq 4 \times 10^{-4}$, and a flux tube of $B = 10^3$ G has an Alfvén velocity of 140 m s^{-1}, consistent with our results.

It is worth noting that our model of flux tube *emergence* omits helicity transport by the "emergence term." The reason for omitting the term is that so little mass can enter the corona, where the density is 10^{-9} times as big as in the convection zone. Instead, the tube's twist drives rotational photospheric flow, which supplies helicity through the "braiding term" of equation (13).

The model makes numerous simplifying assumptions that are intended to be a crude approximation of reality. We characterize the active region field by a single twist α and use a simple estimate of the relative helicity, equation (1), which ignores all of the region's geometry except its polarity separation. Furthermore, we assume the subphotospheric flux tube is thin and has a uniform Alfvén speed. In light of these approximations, we expect the parameters found by our fitting to be only rough estimates of, e.g., the subphotospheric Alfvén speed.

We also made the assumption that the emerging flux tube had been uniformly twisted, $q = \bar{\alpha}/2$, prior to emergence. This assumption allowed us to use simple incident waveforms, $w_{i,\pm} = \bar{\alpha}/4$, in our model of $\alpha(t)$. Had the tube contained some complex pattern of twist $q(s)$, the incident waveforms would be similarly complex. We suggest that the complex time history of α observed in AR 9193 is evidence of such a complex twist pattern. The time history consists of a period of latency (0.5 days $< t <$ 1.1 days), followed by rapid increase (1.1 days $< t <$ 2.1 days), and then a decrease. This pattern would occur under the incidence of a waveform that was low, then high, then negative. Such variable twist patterns would occur quite naturally if the twist were introduced by turbulent distortion of the tube's axis as by the Σ-effect (Longcope, Fisher, & Pevtsov 1998).

6. CONCLUSION

By studying the twisted coronal field during the course of emergence, we have found evidence for the subphotospheric origin of magnetic helicity. We quantify the coronal twist in terms of an α-parameter. This is measured by comparing observed coronal structures with extrapolated field lines. Each of the five active region emergences show α beginning at 0 and increasing to a plateau within 1.5 days. We fit these time histories to a model of the emergence of a twisted subphotospheric flux tube. The implication of this fitting is that helicity is generated in the solar interior and transported into the corona through the emergence of twisted flux tubes. The helicity transport across the photosphere occurs primarily because of spinning of the active region polarities driven by magnetic torque from below.

D. W. L. has been supported by NASA through grant NAG5-6110. *SOHO* is a project of international cooperation between ESA and NASA. Data used here from Mees Solar Observatory, University of Hawaii, are produced with the support of NASA grant NAG5-4941 and NASA contract NAS8-40801. We thank the anonymous referee for helpful comments on the manuscript.

REFERENCES

Bao, S., & Zhang, H. 1998, ApJ, 496, L43
Berger, M. A., & Field, G. B. 1984, J. Fluid Mech., 147, 133
Berger, M. A., & Ruzmaikin, A. 2000, J. Geophys. Res., 105, 10481
Berger, T., & Lites, B. W. 2003, Sol. Phys., 213, 213
Bevington, P. R., & Robinson, D. K. 1992, Data Reduction and Error Analysis for the Physical Sciences (2d ed.; Boston: McGraw-Hill)
Burnette, A. B., Canfield, R. C., & Pevtsov, A. A. 2003, ApJ, submitted
Chae, J. 2001, ApJ, 560, L95
Delaboudinière, J.-P., et al. 1995, Sol. Phys., 162, 291
Démoulin, P., Mandrini, C. H., van Driel-Gesztelyi, L., Thompson, B., Plunkett, S., Kővári, Z., Aulanier, G., & Young, A. 2002, A&A, 382, 650
DeVore, C. R. 2000, ApJ, 539, 944
Domingo, V., Fleck, B., & Poland, A. I. 1995, Sol. Phys., 162, 1
Emonet, T., & Moreno-Insertis, F. 1998, ApJ, 492, 804
Fan, Y., Zweibel, E. G., & Lantz, S. R. 1998, ApJ, 493, 480
Green, L. M., López Fuentes, M. C., Mandrini, C. H., Démoulin, P., van Driel-Gesztelyi, L., & Culhane, J. L. 2002, Sol. Phys., 208, 43
Grigoryev, V. M., & Ermakova, L. V. 2002, Sol. Phys., 207, 309
Kusano, K., Maeshiro, T., Yokoyama, T., & Sakurai, T. 2002, ApJ, 577, 501
Leka, K. D., Canfield, R. C., McClymont, A. N., & van Driel-Gesztelyi, L. 1996, ApJ, 462, 547
Longcope, D. W., Fisher, G. H., & Pevtsov, A. A. 1998, ApJ, 507, 417
Longcope, D. W., & Klapper, I. 1997, ApJ, 488, 443
Longcope, D. W., Linton, M. G., Pevtsov, A. A., Fisher, G. H., & Klapper, I. 1999, in Magnetic Helicity in Space and Laboratory Plasmas, ed. M. R. Brown, R. C. Canfield, & A. A. Pevtsov (Geophys. Monogr. 111; Washington, DC: AGU), 93
Longcope, D. W., & Pevtsov, A. A. 2003, Adv. Space Res., in press
Longcope, D. W., & Welsch, B. T. 2000, ApJ, 545, 1089
Mickey, D. L. 1985, Sol. Phys., 97, 223
Moon, Y.-J., Chae, J., Choe, G. S., Wang, H., Park, Y. D., Yun, H. S., Yurchyshyn, V., & Goode, P. R. 2002, ApJ, 574, 1066
Nindos, A., & Zhang, H. 2002, ApJ, 573, L133
Pevtsov, A. A., Canfield, R. C., & McClymont, A. N. 1997, ApJ, 481, 973
Pevtsov, A. A., Canfield, R. C., & Metcalf, T. R. 1995, ApJ, 440, L109
Portier-Fozzani, F., Aschwanden, M., Démoulin, P., Neupert, W., Delaboudinière, J.-P., & The EIT Team. 2001, Sol. Phys., 203, 289
Press, W. H., Flannery, B. P., Teukolsky, S. A., & Vetterling, W. T. 1986, Numerical Recipes: The Art of Scientific Computing (Cambridge: Cambridge Univ. Press)
Scherrer, P. H., et al. 1995, Sol. Phys., 162, 129